

Generative AI-enhanced Probabilistic Multi-Fidelity Surrogate Modeling Via Transfer Learning

Jice Zeng^a, David Barajas-Solano^{a,*}, Hui Chen^b

^a*Pacific Northwest National Laboratory, Richland, 99352, WA, USA,*

^b*School of Civil Engineering Architecture, Wuhan University of Technology, WuHan, China, 430070,*

Abstract

The performance of machine learning surrogates is critically dependent on data quality and quantity. This presents a major challenge, as high-fidelity (HF) data is often scarce and computationally expensive to acquire, while low-fidelity (LF) data is abundant but less accurate. To address this data-scarcity problem, we develop a probabilistic multi-fidelity surrogate framework based on generative transfer learning. We employ a normalizing flow (NF) generative model as the backbone, which is trained in two phases: (i) the NF is first pretrained on a large LF dataset to learn a probabilistic forward model; (ii) the pretrained model is then fine-tuned on a small HF dataset, allowing it to correct for LF–HF discrepancies via knowledge transfer. To relax the dimension-preserving constraint of standard bijective NFs, we integrate surjective (dimension-reducing) layers with standard coupling blocks. This architecture enables learned dimension reduction while preserving the ability to train with exact likelihoods. The resulting surrogate provides fast probabilistic predictions with quantified uncertainty and significantly outperforms LF-only baselines while using fewer HF evaluations. We validate the approach on a reinforced concrete slab benchmark, combining many coarse-mesh (LF) simulations with a limited set of fine-mesh (HF) simulations. The proposed model achieves probabilistic predictions with HF accuracy, demonstrating a practical path toward data-efficient, generative AI-driven surrogates for complex engineering systems.

Keywords: Generative AI, multi-fidelity modeling, transfer learning, data

*Correspondence authors.

Email address: David.Barajas-Solano@pnnl.gov (David Barajas-Solano)

1. Introduction

High-fidelity (HF) computer modeling using discretization schemes such as the finite elements (FE) method provides a rigorous framework for analyzing and predicting the behavior of complex engineering systems. Nevertheless, while powerful, querying such HF FE models is often computationally expensive, and this cost becomes prohibitive for tasks requiring thousands of queries, such as uncertainty quantification [1], reliability analysis [2], probabilistic model inversion [3, 4, 5], and Bayesian model updating [6, 7], among others. Data-driven deep learning-based surrogates have emerged as an effective approach to accelerating these computations. However, these models face their own critical challenge, namely that the performance of deep learning methods is highly dependent on the quality and quantity of available training data [8, 9].

Training data for surrogate modeling is typically generated from model queries, which can often be performed at different levels of fidelity. Low-fidelity (LF) models, which may employ coarse meshes or simplified physics, are computationally inexpensive and can generate large training datasets quickly. However, these simplifications often introduce significant bias, limiting the surrogate's predictive accuracy. HF models, on the other hand, introduce less bias, but generating sufficiently large training datasets with such models is computationally demanding, leading to a cost-versus-bias trade-off: relying solely on LF data leads to inaccurate surrogates, while relying on HF data is computationally intractable. This challenge motivates the development of multi-fidelity surrogate modeling, a strategy that fuses abundant, inexpensive LF data with scarce, costly HF data to achieve HF accuracy [10, 11]. For instance, Feng et al. [12] proposed an ANN-based multi-fidelity deep learning framework to improve the efficiency of seismic structural analysis. Stavropoulou et al. [13] developed an LSTM-based multi-fidelity surrogate modeling approach for predicting nonlinear responses of multiple wave energy converters. Yang et al. [14] introduced a multi-fidelity DeepONet framework capable of efficiently predicting spatio-temporal flow fields with significantly fewer high-fidelity data. Similarly, Zhong et al. [15] presented a hybrid deep learning-enabled multi-fidelity framework to enhance time-series prediction in structural dynamic analysis. Zeng et al. [16] also proposed

a multi-fidelity temporal convolutional network (TCN) model for response prediction of vehicle crash tests. Although these methods demonstrate notable improvements in predictive accuracy and computational efficiency when compared to baseline models trained solely on LF data, they remain fundamentally deterministic. As a result, they do not provide any quantification of predictive uncertainty, which is critical for risk-informed decision-making and reliability assessment in high-stakes engineering applications.

To address this gap, a separate line of research has focused on probabilistic multi-fidelity modeling. However, existing approaches present their own set of challenges. For example, He et al. [17] proposed a multi-fidelity residual Gaussian process (GP) framework to probabilistically identify geomaterial properties. However, GP models are sensitive to kernel selection and hyperparameter estimation. Wang et al. [18] introduced a physics-guided generative adversarial network (GAN) for fatigue life prediction, where uncertainty in fatigue performance was also quantified. Nevertheless, GANs are notoriously difficult to train, often suffering from instability and mode collapse. More recently, Xie et al. [19] proposed a multi-fidelity Bayesian neural network (BNN) framework for aerodynamic modeling, where Hamiltonian Monte Carlo (HMC) was employed to estimate the posteriors of BNN hyperparameters. However, HMC is computationally expensive and scales poorly with the dimensionality of the parameter space. These limitations highlight a clear need for a multi-fidelity surrogate framework that is both probabilistic and computationally tractable, capable of providing robust uncertainty quantification without the training instabilities of GAN or the high computational overhead of traditional sampling-based approximate Bayesian inference methods.

Recent advances in generative artificial intelligence (AI) offer a promising new direction for probabilistic surrogate modeling. Generative AI models have demonstrated a remarkable capacity for learning high-dimensional probability distributions, capturing complex nonlinear relationships, and generating realistic synthetic data across domains like computer vision [20], natural language processing [21], and scientific machine learning [3]. These capabilities are uniquely suited to address the key challenges in probabilistic multi-fidelity modeling. First, as inherently probabilistic models, generative methods naturally quantify predictive uncertainty. Second, they can flexibly represent complex, nonlinear relationships between LF and HF data. Third, through deep neural architectures, generative AI is well-suited to handle high-dimensional input-output spaces (e.g., spatio-temporal fields, time-series re-

sponses), where probabilistic surrogates such as sampling-based BNN models often become computationally intractable. These properties make generative models a compelling foundation for developing robust probabilistic multi-fidelity surrogate frameworks. Nevertheless, despite this clear potential, the application of generative modeling to multi-fidelity surrogate modeling remains limited. To the best of the authors' knowledge, existing studies have primarily focused on traditional deep learning frameworks, with relatively few efforts dedicated to leveraging the power of generative AI.

To address this gap, this study proposes a generative AI-enhanced probabilistic multi-fidelity surrogate modeling framework. Our approach is designed in two stages: first, a generative surrogate is pretrained on abundant LF data to learn a foundational probabilistic model; second, the model is fine-tuned using limited HF data via transfer learning, enabling it to capture complex LF–HF relationships. The proposed framework employs surjective normalizing flows (NFs), a dimension-reducing variant of flow-based generative models. Unlike conventional NF, which are constrained to preserve input dimensionality in the latent space, surjective NF integrates both surjective and bijective layers within a unified neural architecture. The surjective layers project high-dimensional responses onto a lower-dimensional latent space, while the bijective layers ensure invertibility where needed, allowing exact density evaluation and tractable likelihood estimation. This hybrid property enables surjective NF to effectively handle high-dimensional responses such as time-series data, while providing the ability to train and evaluate the model on time-series data and perform uncertainty quantification. The proposed multi-fidelity framework is applied to surrogate modeling of the time-series response of a reinforced concrete slab structure. The LF data are generated from a coarse-mesh FE model, whereas the HF data are obtained from a fine-mesh model. To evaluate the robustness of the framework, different levels of correlation between LF and HF data, as well as the effect of varying the amount of HF data, are systematically investigated. The results demonstrate that the proposed approach achieves efficient, HF-accurate probabilistic response predictions.

The remainder of this paper is organized as follows: in Sec. 2 we formulate the data-driven multi-fidelity surrogate modeling problem, and describe the proposed generative transfer learning approach we take to solve this problem. In Sec. 3 we describe the NF architecture for the probabilistic surrogate modeling, and in Sec. 4 we present a case study analyzing the performance of the framework under different levels of LF–HF data correlation and the effect

of varying the number of HF training samples. In addition, we also benchmark the method against a TCN baseline [15, 16]. Finally, we summarize our conclusions and outline future research directions in Sec. 5.

2. Probabilistic multi-fidelity surrogate modeling framework

2.1. Problem formulation

We restrict our attention in this work to the bi-fidelity setting. Let $m, n \in \mathbb{N}$, and let $\Theta := \mathbb{R}^m$ and $Y := \mathbb{R}^n$ denote the space of model parameters and the space of model outputs, respectively. In this work we consider the problem of learning a surrogate model of the functional relation $G: \Theta \rightarrow Y$ between model parameters and model outputs from data. To generate the training data, we assume there is a data-generating distribution of model parameters $p(\boldsymbol{\theta})$ and that we have access to two data-generating models: an LF model $G_{\text{LF}}: \Theta \rightarrow Y$, and a HF model $G_{\text{HF}}: \Theta \rightarrow Y$. Here we assume for simplicity that both the LF and HF outputs are in Y . These models define the data-generating distributions $p_{\text{LF}}(\mathbf{y}, \boldsymbol{\theta})$ and $p_{\text{HF}}(\mathbf{y}, \boldsymbol{\theta})$, respectively.

Furthermore, we assume that the expected prediction error of the HF model with respect to the true model G , $\mathbb{E}_{p(\boldsymbol{\theta})}|G_{\text{HF}}(\boldsymbol{\theta}) - G(\boldsymbol{\theta})|$, is negligible, that the LF model is significantly biased, and that it is much computationally faster to sample from the LF data-generating distribution than from the HF data-generating distribution. Therefore, our goal is to learn a model for $p_{\text{HF}}(\mathbf{y} \mid \boldsymbol{\theta})$ by using both an LF dataset $\mathcal{D}_{\text{LF}} := \{\mathbf{y}_{\text{LF}}^{(i)}, \boldsymbol{\theta}^{(i)}\}_{i=1}^{N_{\text{LF}}} \sim p_{\text{LF}}(\mathbf{y}, \boldsymbol{\theta})$ and a HF dataset $\mathcal{D}_{\text{HF}} := \{\mathbf{y}_{\text{HF}}^{(i)}, \boldsymbol{\theta}^{(i)}\}_{i=1}^{N_{\text{HF}}} \sim p_{\text{HF}}(\mathbf{y}, \boldsymbol{\theta})$, with $N_{\text{LF}} \gg N_{\text{HF}}$.

2.2. Multi-fidelity generative modeling via transfer learning

To solve this probabilistic multi-fidelity surrogate modeling problem we propose the framework illustrated in Fig. 1. This framework consists of two stages: pre-training and fine-tuning. Both stages employ surjective NF models as the backbone, which function as probabilistic forward surrogates by approximating the conditional distributions $p_{\text{LF}}(\mathbf{y} \mid \boldsymbol{\theta})$ and $p_{\text{HF}}(\mathbf{y} \mid \boldsymbol{\theta})$.

In the pre-training stage, the LF dataset is used to train a surjective NF to approximate $p_{\text{LF}}(\mathbf{y} \mid \boldsymbol{\theta})$. This stage establishes a foundational generative model that captures the general behavior and response distributions of the low-fidelity system. In the fine-tuning stage, we utilize the smaller HF dataset to fine-tune the pre-trained LF model and correct for the biases inherent in the LF data, resulting in a model approximating $p_{\text{HF}}(\mathbf{y} \mid \boldsymbol{\theta})$.

A key advantage of this generative approach is that the resulting surrogate provides a full probabilistic distribution for any given input model parameters, rather than a single-point estimate. The proposed framework thus effectively addresses data scarcity by fusing abundant LF data with limited HF data. This process yields an accurate, uncertainty-aware surrogate that captures HF-level physics while significantly reducing the computational burden associated with extensive HF simulations.

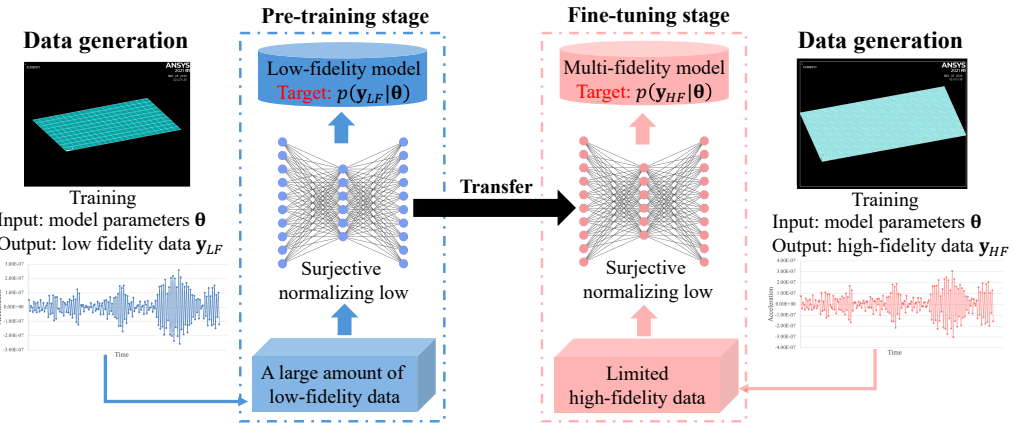


Figure 1: Workflow of the proposed probabilistic multi-fidelity surrogate modeling framework.

Let $q(\mathbf{y} | \boldsymbol{\theta}, \boldsymbol{\phi})$ denote the parameterized surjective NF model, where $\boldsymbol{\phi}$ denotes the model parameters. In the pre-training stage, we learn the LF model by maximizing the expectation of the surjective NF model's likelihood over the LF data, that is,

$$\boldsymbol{\phi}_{\text{LF}}^* = \arg \max_{\boldsymbol{\phi}} \mathbb{E}_{(\mathbf{y}, \boldsymbol{\theta}) \sim \mathcal{D}_{\text{LF}}} \log q(\mathbf{y} | \boldsymbol{\theta}, \boldsymbol{\phi}). \quad (1)$$

This step extracts the dominant structural patterns that are already well captured at the LF level. Next, in the fine-tuning stage we transfer knowledge from the LF model to the MF model by using the LF-trained parameters $\boldsymbol{\phi}_{\text{LF}}^*$ as the initial guess for the parameters of the MF model, and then fine-tuning the MF model by maximizing its likelihood over the HF data, that is,

$$\boldsymbol{\phi}_{\text{MF}}^* = \arg \max_{\boldsymbol{\phi}} \mathbb{E}_{(\mathbf{y}, \boldsymbol{\theta}) \sim \mathcal{D}_{\text{HF}}} \log q_{\boldsymbol{\phi}}(\mathbf{y} | \boldsymbol{\theta}). \quad (2)$$

where $\boldsymbol{\phi}_{\text{MF}}^*$ denotes the optimal parameters of the final MF model.

Once trained, the MF surrogate can be queried for any new input $\boldsymbol{\theta}^*$. Specifically, we use Monte Carlo sampling to generate samples from the predictive distribution $q(\mathbf{y} \mid \boldsymbol{\theta}^*, \boldsymbol{\phi}_{\text{MF}}^*)$, which are then employed to estimate the predictive mean and variance, credibility intervals (CIs), and other statistics of interest. This enables the surrogate not only to generate accurate HF predictions but also to quantify predictive uncertainty.

3. NF-based probabilistic surrogate models

The core of our proposed framework is the surjective conditional NF model employed to approximate conditional distributions of the form $p(\mathbf{y} \mid \boldsymbol{\theta})$. Surjective NFs extend the traditional NF architecture by integrating dimension-reducing (surjective) layers together with standard bijective transformations. This hybrid design is key to enabling scalable modeling of high-dimensional responses such as time-series data, a task that is often intractable for standard NF. To provide the necessary background, we first review bijective conditional NFs before describing the surjective architecture we employ in this work.

3.1. Bijective conditional NFs

Conditional NFs construct the conditional distribution $p(\mathbf{y} \mid \boldsymbol{\theta})$ by transporting a simple base density $p_{\mathbf{z}}(\mathbf{z})$ (with $\mathbf{z} \in \mathbb{R}^n$, typically $\mathcal{N}(\mathbf{0}, \mathbf{I}_n)$) through a parameterized invertible, $\boldsymbol{\theta}$ -dependent map [22], that is,

$$\mathbf{z} = f(\mathbf{y}; \boldsymbol{\theta}, \boldsymbol{\phi}), \quad \mathbf{y} = f^{-1}(\mathbf{z}; \boldsymbol{\theta}, \boldsymbol{\phi}), \quad \mathbf{z} \sim p_{\mathbf{z}}(\mathbf{z}), \quad (3)$$

where $f(\cdot; \boldsymbol{\theta}, \boldsymbol{\phi})$ denotes the parameterized $\mathbf{y} \rightarrow \mathbf{z}$ invertible transformation, $f^{-1}(\cdot; \boldsymbol{\theta}, \boldsymbol{\phi})$ its inverse, and $\boldsymbol{\phi}$ its parameters. In practice, f is constructed by composing K invertible bijections $\{f_k\}_{k=1}^K$, that is, we employ the sequence of transformations

$$\mathbf{y} := \mathbf{z}_0 \rightarrow \mathbf{z}_1 \rightarrow \cdots \rightarrow \mathbf{z}_{K-1} \rightarrow \mathbf{z}_K := \mathbf{z},$$

where the \mathbf{z}_k s are given by

$$\mathbf{z}_k = f_k(\mathbf{z}_{k-1}; \boldsymbol{\theta}, \boldsymbol{\phi}), \quad k = 1, \dots, K. \quad (4)$$

Applying the multivariate change-of-variables formula to Eqs. (3) and (4) leads to the closed-form expression for $p(\mathbf{y} \mid \boldsymbol{\theta})$

$$p(\mathbf{y} \mid \boldsymbol{\theta}, \boldsymbol{\phi}) = p_{\mathbf{z}}(\mathbf{z}_K) \prod_{k=1}^K \left| \det \frac{\partial f_k}{\partial \mathbf{z}_{k-1}} (\mathbf{z}_{k-1}; \boldsymbol{\theta}, \boldsymbol{\phi}) \right|, \quad (5)$$

or, in log form,

$$\log p(\mathbf{y} \mid \boldsymbol{\theta}, \boldsymbol{\phi}) = \log p_{\mathbf{z}}(\mathbf{z}_K) + \sum_{k=1}^K \log \left| \det \frac{\partial f_k}{\partial \mathbf{z}_{k-1}}(\mathbf{z}_{k-1}; \boldsymbol{\theta}) \right|. \quad (6)$$

The components of the flow transformation are chosen so that each log-determinant term is inexpensive to evaluate (e.g., via triangular Jacobians), yielding an explicit, tractable closed-form expression for the log-likelihood as a function of the flow parameters $\boldsymbol{\phi}$.

Given training data $\mathcal{D} := \{(\mathbf{y}^{(i)}, \boldsymbol{\theta}^{(i)})\}_{i=1}^N$, the flow parameters $\boldsymbol{\phi}$ are estimated by maximizing the expected log-likelihood over the training data, that is,

$$\begin{aligned} \mathcal{L}(\boldsymbol{\phi}) &= \mathbb{E}_{(\mathbf{y}, \boldsymbol{\theta}) \sim \mathcal{D}} [\log p(\mathbf{y}^{(i)} \mid \boldsymbol{\theta}^{(i)}, \boldsymbol{\phi})] \\ &= \mathbb{E}_{(\mathbf{y}, \boldsymbol{\theta}) \sim \mathcal{D}} \left[\log p_{\mathbf{z}}(f(\mathbf{y}^{(i)}; \boldsymbol{\theta}^{(i)}, \boldsymbol{\phi})) + \sum_{k=1}^K \log \left| \det \frac{\partial f_k(\mathbf{z}_{k-1}; \boldsymbol{\theta}^{(i)}, \boldsymbol{\phi})}{\partial \mathbf{z}_{k-1}} \right| \right], \end{aligned} \quad (7)$$

which is performed via stochastic gradient methods.

To generate predictions for a new input $\boldsymbol{\theta}^*$, we employ the sampling procedure implied by Eq. (3), that is, to draw samples from the distribution of latent codes, $\mathbf{z} \sim p_{\mathbf{z}}$, and apply the inverse transformation $f^{-1}(\mathbf{z}; \boldsymbol{\theta}^*, \boldsymbol{\phi})$, to these samples, resulting in an ensemble of draws from the predictive distribution $p(\mathbf{y} \mid \boldsymbol{\theta}^*, \boldsymbol{\phi})$. These generated samples can then be used to compute statistics of the predictive distribution such as mean, variance, and predictive means, among others, and thus provide a complete probabilistic forecast.

A critical limitation of the NF described above is their dimension-preserving property. Defining the flow in terms of a sequence of bijective transformations mandates that the latent space \mathbf{z} must have the same dimension as the data space \mathbf{y} . This property becomes computationally prohibitive and inefficient when modeling high-dimensional structural responses, such as time-series data. To address this bottleneck, we propose employing surjective NFs to construct the proposed multifidelity probabilistic surrogates. This architecture explicitly augments the standard bijective stack with dimension-reducing (surjective) maps, enabling the model to efficiently compress the high-dimensional response into a low-dimensional latent representation, thereby enhancing scalability for modeling high-dimensional responses.

3.2. Surjective conditional NFs

The surjective NF extends the classical framework of bijective flows by allowing mappings that reduce dimensionality, bridging the gap between NF and variational autoencoder. This design of surjective NF enables scalable likelihood-based training even when modeling high-dimensional responses, where strict bijections may be inefficient or inexpressive. The formulation is inspired within the broader generative framework of Nielsen et al. (2020) [23], in which the log-likelihood of data is decomposed into contributions from bijective and surjective layers, combining base densities, Jacobian corrections, and stochastic decoders.

Let again $\mathbf{y} \in \mathbb{R}^W$ denote an output datum and introduce a latent variable $\mathbf{z} \in \mathbb{R}^Q$, $Q \leq W$, with a base distribution $p_{\mathbf{z}}(\mathbf{z})$. Furthermore, we relate \mathbf{z} and \mathbf{y} via the surjective map $h: \mathbb{R}^W \rightarrow \mathbb{R}^Q$, $\mathbf{z} = h(\mathbf{y}; \boldsymbol{\theta})$, parameterized by the input data $\boldsymbol{\theta}$ (contrast with Eq. (3), where the $\mathbf{y} \rightarrow \mathbf{z}$ is bijective.) Given that the $\mathbf{y} \rightarrow \mathbf{z}$ is not bijective, we cannot employ the change-of-variables formula to derive a closed-form expression for $\log p(\mathbf{y} \mid \boldsymbol{\theta})$ as in Eq. (6). Instead, in the SurVAE framework, we consider the inverse of the surjection h to be a stochastic transformation $p(\mathbf{y} \mid \mathbf{z}, \boldsymbol{\theta})$, and the log-likelihood of the output data is modeled in terms of the stochastic and surjective maps as [23, 24]

$$\log p(\mathbf{y} \mid \boldsymbol{\theta}) = \log p_{\mathbf{z}}(\mathbf{z}) + V(\mathbf{y}, \mathbf{z} \mid \boldsymbol{\theta}) + E(\mathbf{y}, \mathbf{z} \mid \boldsymbol{\theta}), \quad \mathbf{z} \sim q(\mathbf{z} \mid \mathbf{y}, \boldsymbol{\theta}), \quad (8)$$

where $q(\mathbf{z} \mid \mathbf{y})$, $\boldsymbol{\theta}$ is a variational distribution, $E(\mathbf{y}, \mathbf{z})$ denotes the variational bound looseness, and $V(\mathbf{y}, \mathbf{z})$ denotes the “likelihood contribution”, given by

$$V(\mathbf{y}, \mathbf{z} \mid \boldsymbol{\theta}) = \lim_{q(\mathbf{z} \mid \mathbf{y}) \rightarrow \delta(\mathbf{z} - h(\mathbf{y}; \boldsymbol{\theta}))} \mathbb{E}_{q(\mathbf{z} \mid \mathbf{y})} \left[\log \frac{p(\mathbf{y} \mid \mathbf{z}, \boldsymbol{\theta})}{q(\mathbf{z} \mid \mathbf{y}, \boldsymbol{\theta})} \right]. \quad (9)$$

The bound looseness term vanishes if the so-called “right inverse condition” is satisfied [25, 23], that is, if $p(\mathbf{y} \mid \mathbf{y}, \boldsymbol{\theta})$ defines a distribution over the possible right inverses of the surjection h .

It remains to formulate the surjective layer architecture by constructing the surjection $\mathbf{y} \rightarrow \mathbf{z}$ and the stochastic transformation $\mathbf{z} \rightarrow \mathbf{y}$. To do so, we split \mathbf{y} into discarded and kept blocks:

$$\mathbf{y} = \begin{bmatrix} \mathbf{y}^- \\ \mathbf{y}^+ \end{bmatrix}, \quad \mathbf{y}^- \in \mathbb{R}^{W-Q}, \quad \mathbf{y}^+ \in \mathbb{R}^Q, \quad 0 < Q < W. \quad (10)$$

and define a conditional bijection on the kept block

$$f: \mathbb{R}^Q \rightarrow \mathbb{R}^Q, \quad \mathbf{y}^+ = f(\mathbf{z}; \mathbf{y}^-, \boldsymbol{\theta}), \quad \mathbf{z} = f^{-1}(\mathbf{y}^+; \mathbf{y}^-, \boldsymbol{\theta}), \quad (11)$$

where f is any tractable flow transform (e.g., coupling or autoregressive) conditional on $(\mathbf{y}^-, \boldsymbol{\theta})$. Intuitively, the pair $(\mathbf{y}^-, \boldsymbol{\theta})$ selects a bijection acting on \mathbf{y}^+ . Therefore, in the $\mathbf{y} \rightarrow \mathbf{z}$, the surjective layer splits \mathbf{y} into blocks as in Eq. (10) and deterministically generates \mathbf{z} from the blocks using the flow transformation f as in Eq. (11). In the $\mathbf{z} \rightarrow \mathbf{y}$ direction, a surjective layer then: (i) stochastically generates \mathbf{y}^- by sampling from the stochastic “decoder” $p(\mathbf{y}^- | \mathbf{z}, \boldsymbol{\theta})$, and (ii) deterministically generates \mathbf{y}^+ using the flow transformation f as in Eq. (11).

Based on this construction, it can be said that the conditional likelihood factorizes the distribution of the outputs into a stochastic decoder on the discarded block and a Dirac delta distribution on the kept block, that is,

$$p(\mathbf{y} | \mathbf{z}, \boldsymbol{\theta}) = p(\mathbf{y}^- | \mathbf{z}, \boldsymbol{\theta}) \delta(\mathbf{y}^+ - f(\mathbf{z}; \mathbf{y}^-, \boldsymbol{\theta})). \quad (12)$$

Furthermore, limiting distribution for the variational density is given by the Dirac delta change-of-variables rule as

$$\begin{aligned} q(\mathbf{z} | \mathbf{y}) &\rightarrow \delta(\mathbf{z} - f^{-1}(\mathbf{y}^+; \mathbf{y}^-, \boldsymbol{\theta})) \\ &= \delta(\mathbf{y}^+ - f(\mathbf{z}; \mathbf{y}^-, \boldsymbol{\theta})) |\det J^{-1}|^{-1}, \end{aligned} \quad (13)$$

where $J(\mathbf{z}; \mathbf{y}^-, \boldsymbol{\theta}) = \partial f(\mathbf{z}; \mathbf{y}^-, \boldsymbol{\theta}) / \partial \mathbf{z}$ is the Jacobian of the flow transformation. Substituting Eq. (12)–Eq. (13) into Eq. (9), the likelihood contribution is expressed as [25]

$$\begin{aligned} V(\mathbf{y}, \mathbf{z} | \boldsymbol{\theta}) &= \int d\mathbf{z} \delta(\mathbf{z} - f^{-1}(\mathbf{y}^+; \mathbf{y}^-, \boldsymbol{\theta})) \log \left[\frac{p(\mathbf{y}^- | \mathbf{z}, \boldsymbol{\theta}) \delta(\mathbf{y}^+ - f(\mathbf{z}; \mathbf{y}^-, \boldsymbol{\theta}))}{\delta(\mathbf{y}^+ - f(\mathbf{z}; \mathbf{y}^-, \boldsymbol{\theta})) |\det J^{-1}|^{-1}} \right] \\ &= \log p(\mathbf{y}^- | \mathbf{z}, \boldsymbol{\theta}) - \log |\det J(\mathbf{z}; \mathbf{y}^-, \boldsymbol{\theta})|, \quad \text{s.t. } \mathbf{y}^+ = f(\mathbf{z}; \mathbf{y}^-, \boldsymbol{\theta}). \end{aligned} \quad (14)$$

For this construction, the looseness term vanishes [25]. Therefore, Eq. (8) becomes

$$\begin{aligned} \log p(\mathbf{y} | \boldsymbol{\theta}) &= \log p_{\mathbf{z}}(\mathbf{z}) + V(\mathbf{y}, \mathbf{z}) \\ &= \underbrace{\log p_{\mathbf{z}}(\mathbf{z})}_{\text{base}} + \underbrace{\log p(\mathbf{y}^- | \mathbf{z}, \boldsymbol{\theta})}_{\text{decoder on discarded}} - \underbrace{\log |\det J(\mathbf{z}; \mathbf{y}^-, \boldsymbol{\theta})|}_{\text{kept-block Jacobian}}, \quad (15) \\ &\text{s.t. } \mathbf{y}^+ = f(\mathbf{z}; \mathbf{y}^-, \boldsymbol{\theta}). \end{aligned}$$

This formula is then used to compute the single-layer likelihood during training and inference. In this work, we employ the decoder architecture

$$p_\phi(\mathbf{y}^- \mid \mathbf{z}, \boldsymbol{\theta}, \boldsymbol{\phi}) := \mathcal{N}(\mu_\phi(\mathbf{z}; \boldsymbol{\theta}), \text{diag}(\exp(2\sigma_\phi(\mathbf{z}; \boldsymbol{\theta})))) , \quad (16)$$

where the functions μ_ϕ and σ_ϕ are the output of a multilayer perceptron parameterized by $\boldsymbol{\phi}$.

We now proceed to integrate the surjective layers defined above with bijective layers. For evaluating the likelihood of a given output \mathbf{y} , we evaluate a K -layer flow consisting of both bijective (dimension-preserving) and surjective (dimension-reducing) layers. We work backwards through these layers to the base latent variable $\mathbf{z}_0 \sim p_0$. To avoid overloading the symbol \mathbf{z} , which is reserved for lower-dimensional end of surjective layers, we denote the intermediate flow states by $\mathbf{y} \equiv \mathbf{u}_K, \mathbf{u}_{K-1}, \dots, \mathbf{u}_1, \mathbf{u}_0 \equiv \mathbf{z}_0$. We partition the layer indices into bijective and surjective layer indices as

$$\mathcal{B} = \{\text{bij. layers}\}, \mathcal{S} = \{\text{surj. layers}\}, \mathcal{B} \cap \mathcal{S} = \emptyset, \mathcal{B} \cup \mathcal{S} = \{1, \dots, K\}. \quad (17)$$

Finally, it follows that if the k th layer is surjective, then $\mathbf{z}_k := \mathbf{u}_{k-1}$, that is, the lower-dimensional end of the surjection corresponds to the previous layer's state.

Bijective layers employ the parameterized bijection $\mathbf{u}_{k-1} = f_k^{-1}(\mathbf{u}_k; \boldsymbol{\theta}, \boldsymbol{\phi})$ and contribute only the standard change-of-variables Jacobian. Let $J_k^{(\text{bij})} = \partial f_k(\mathbf{u}_{k-1}; \boldsymbol{\theta}, \boldsymbol{\phi}) / \partial \mathbf{u}_{k-1}$. This contribution takes the form

$$C_k^{(\text{bij})} = -\log \left| \det J_k^{(\text{bij})} \right|_{\mathbf{u}_{k-1} = f_k^{-1}(\mathbf{u}_k; \boldsymbol{\theta}, \boldsymbol{\phi})}. \quad (18)$$

A surjection splits the state into kept and discarded blocks \mathbf{u}_k^+ and \mathbf{u}_k^- , respectively, and employs the parameterized kept-block bijection $f_k(\cdot; \mathbf{u}_k^-, \boldsymbol{\theta}, \boldsymbol{\phi})$ and the decoder $p_k(\cdot \mid \mathbf{z}_k, \boldsymbol{\theta}, \boldsymbol{\phi})$. Define

$$\mathbf{z}_k = f_k^{-1}(\mathbf{u}_k^+; \mathbf{u}_k^-, \boldsymbol{\theta}, \boldsymbol{\phi}), \quad J_k^{(\text{surj})} = \partial f_k(\mathbf{z}_k; \mathbf{u}_k^-, \boldsymbol{\theta}, \boldsymbol{\phi}) / \partial \mathbf{z}_k. \quad (19)$$

From Eq. (15), surjective layers contribute both a decoder log-density for the discarded block and a kept-block Jacobian term. These contributions take the form

$$C_k^{(\text{surj})} = \log p_k(\mathbf{u}_k^- \mid \mathbf{z}_k, \boldsymbol{\theta}, \boldsymbol{\phi}) - \log \left| \det J_k^{(\text{surj})} \right|, \quad \mathbf{u}_{k-1} := \mathbf{z}_k. \quad (20)$$

Collecting the contributions from all layers $k = K, \dots, 1$ yields the log-conditional likelihood of the output \mathbf{y} given an input θ :

$$\log q(\mathbf{y} \mid \boldsymbol{\theta}, \boldsymbol{\phi}) = \underbrace{\log p_0(\mathbf{u}_0)}_{\text{base density}} + \sum_{k \in \mathcal{B}} \underbrace{C_k^{(\text{bij})}}_{\text{Eq. (18)}} + \sum_{k \in \mathcal{S}} \underbrace{C_k^{(\text{surj})}}_{\text{Eq. (20)}}. \quad (21)$$

This expression provides a tractable expression for every training example $(\mathbf{y}, \boldsymbol{\phi})$.

The parameters $\boldsymbol{\phi}$ are estimated by maximizing the expected log-likelihood over a training dataset \mathcal{D} , that is,

$$\mathcal{L}(\boldsymbol{\phi}) := \mathbb{E}_{(\mathbf{y}, \boldsymbol{\theta}) \sim \mathcal{D}} [\log q(\mathbf{y} \mid \boldsymbol{\theta}, \boldsymbol{\phi})], \quad \boldsymbol{\phi}^* := \arg \max_{\boldsymbol{\phi}} \mathcal{L}(\boldsymbol{\phi}). \quad (22)$$

Accordingly, the gradient of the objective is given by

$$\nabla_{\boldsymbol{\phi}} \mathcal{L}(\boldsymbol{\phi}) = \mathbb{E}_{(\mathbf{y}, \boldsymbol{\theta}) \sim \mathcal{D}} \nabla_{\boldsymbol{\phi}} \log q(\mathbf{y} \mid \boldsymbol{\theta}, \boldsymbol{\phi}), \quad (23)$$

which is directly estimated via automatic differentiation through the flow architecture.

4. Application

We apply and validate the proposed multi-fidelity framework on a time-domain structural dynamics problem. The quantity of interest is the time-series acceleration response of a structure under ambient excitation. We consider an elastic structural system with n degrees of freedom, governed by the dynamic equation of motion

$$\mathbf{M}(\boldsymbol{\theta})\ddot{\mathbf{u}}(t, \boldsymbol{\theta}) + \mathbf{C}(\boldsymbol{\theta})\dot{\mathbf{u}}(t, \boldsymbol{\theta}) + \mathbf{K}(\boldsymbol{\theta})\mathbf{u}(t, \boldsymbol{\theta}) = \mathbf{f}(t), \quad (24)$$

where $\mathbf{M}, \mathbf{C}, \mathbf{K} \in \mathbb{R}^{n \times n}$ are the mass, damping, and stiffness matrices, respectively, and $\mathbf{u}, \dot{\mathbf{u}}, \ddot{\mathbf{u}}$ denote the displacement, velocity, and acceleration vectors, respectively. The input parameters $\boldsymbol{\theta}$ represent physical and geometric properties. The excitation $\mathbf{f}(t)$ is modeled as a base-acceleration time history consistent with zero-mean, band-limited Gaussian white noise to simulate ambient vibration.

The validation model is a reinforced-concrete slab modeled in the commercial FE software ANSYS, as shown in Fig. 2. This slab is partitioned

into nine subsections, and the Young’s modulus of each subsection is characterized by a single model parameter, resulting in a total of nine model parameters. Specifically, each parameter represents the relative deviation in Young’s modulus of the corresponding component with respect to its nominal value, that is,

$$\theta_i = \frac{E_i - E_i^{\text{nor}}}{E_i^{\text{nor}}}, \quad i = 1, 2, \dots, 9,$$

where E_i and E_i^{nor} denote the actual and nominal Young’s moduli, respectively. All the input parameters are assumed to follow a uniform distribution, $\theta_i \sim \mathcal{U}(-0.3, 0.3)$.

The two fidelity levels are defined by their mesh discretization, which directly controls the trade-off between cost and accuracy. Namely, the LF model uses a coarse discretization with a characteristic element size of 0.05 m. These simulations are inexpensive, allowing for broad coverage of the parameter space. The HF model uses a fine discretization with a characteristic element size of 0.005 m. These simulations are computationally costly but provide more accurate acceleration response simulations. Apart from the mesh density and any differences specified in the test scenarios below, both models share the same geometric description and boundary conditions.

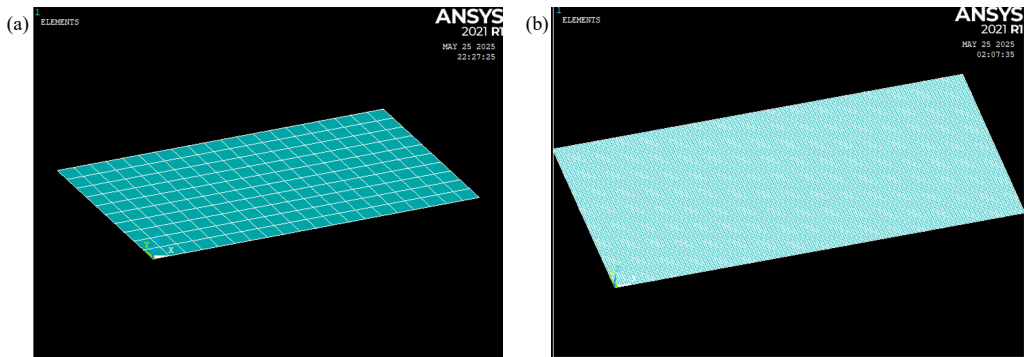


Figure 2: FE model of a reinforced-concrete slab: (a) LF model; (b) HF model.

To generate the datasets, we employ ANSYS’s “Transient Structural Analysis” capabilities. For a given input parameter vector $\boldsymbol{\theta}$, the system matrices $\mathbf{M}(\boldsymbol{\theta})$, $\mathbf{C}(\boldsymbol{\theta})$ (e.g., using Rayleigh damping), and $\mathbf{K}(\boldsymbol{\theta})$ are assembled. A Gaussian white-noise base-acceleration time history is then created based on the chosen time step Δt and simulation duration. Finally, a transient analysis using the Newmark method is performed, producing the time-series

acceleration $\mathbf{y} = \ddot{\mathbf{u}}(t, \boldsymbol{\theta})$ at the specified sensor locations. This process is repeated for all parameter samples to generate the \mathcal{D}_{LF} and \mathcal{D}_{HF} datasets.

To evaluate the robustness of the multi-fidelity surrogate, two distinct scenarios are considered: strong correlation between simulated LF and HF signals (Case 1), and weak correlation between signals (Case 2). In Case 1, the LF and HF models differ only in their mesh density (0.05 m vs. 0.005 m). All other modeling settings, including the external excitation $\mathbf{f}(t)$, are identical, so that the resulting LF and HF acceleration responses exhibit a strong correlation, and discrepancies are dominated by spatial discretization errors. Case 2 introduces a more significant discrepancy between the models: In addition to the mesh refinement, the LF and HF simulations are subjected to different external excitations. For instance, the LF responses may be generated under a simplified loading (e.g., harmonic or band-limited white noise), while the HF responses are produced under a more realistic and complex transient or stochastic excitation. In this application, the discrepancy between the LF and HF excitations is introduced through a controlled perturbation of the excitation amplitude, that is,

$$\mathbf{f}_{\text{HF}}(t) = \mathbf{f}_{\text{LF}}(t)(1 + F_{\Delta}), \quad F_{\Delta} \sim \mathcal{U}(-0.6, 0.6),$$

which leads to weakened correlation between the LF and HF responses and a more challenging and realistic transfer learning scenario.

4.1. Case 1: strong correlation between HF and LF data

To emulate a realistic data-imbalance setting, we generate 1,000 LF and 200 HF acceleration time-series data pairs. The data generation required 4.52 hours for the LF simulations and 13.47 hours for the HF simulations. The responses are sampled at 20 Hz over a 10 seconds window. Fig. 3 presents an example with strong LF–HF correlation: the LF signal shows modest amplitude/phase deviations from the HF reference, and both traces follow similar temporal patterns.

As discussed in Sec. 2.2, the LF model is first trained using 980 LF data pairs, with the remaining samples used for validation. The surjective flow model consists of seven layers, with dimensionalities [200, 200, 200, 200, 10, 10, 10]. The first four layers are dimension-preserving, while the fifth layer performs a dimensionality reduction from $W = 200$ to $Q = 10$, corresponding to a reduction factor of 95%. The final two layers operate bijectively. The rationale behind this architecture is that the dataset is fully processed

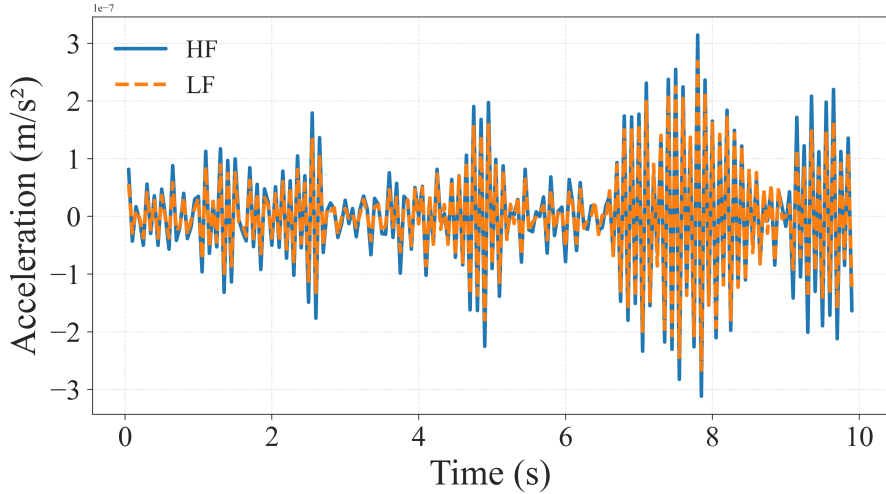


Figure 3: Example of simulated LF and HF acceleration responses for Case 1.

through bijective mappings before data compression, ensuring that sufficient structure is extracted prior to dimensionality reduction. Subsequent bijective refinement after reduction is aimed to balance expressiveness with efficiency.

The bijective layers are implemented using masked coupling transformations [26], where alternating binary masks and permutations are applied at successive layers. The surjective component of the flow is realized at the fifth layer, where dimensionality reduction is introduced through a funnel layer [25], implemented using the SURJECTORS library [27]. Finally, the sixth and seventh layers are also bijective masked coupling transformations. For training, optimization is performed using the Adam algorithm [28] with a fixed learning rate of 10^{-4} . A batch size of 64 is used throughout, and training is performed for 1,000 epochs.

Fig. 4 presents the validation performance of the trained LF model. The left panel compares the reconstructed LF response against the true LF time history for a representative case. The predicted mean response aligns well with the simulated data, and the shaded region indicates the 95% CI. The narrow width of the CI demonstrates that the model not only captures the correct temporal pattern but also maintains low predictive uncertainty. The coefficient of determination, $R^2 = 0.9998$, further confirms the good agreement between the estimated and true LF responses. The right panel shows a scatter plot of predicted versus true LF values. The points cluster tightly around the reference line $y = x$, indicating highly accurate predictions.

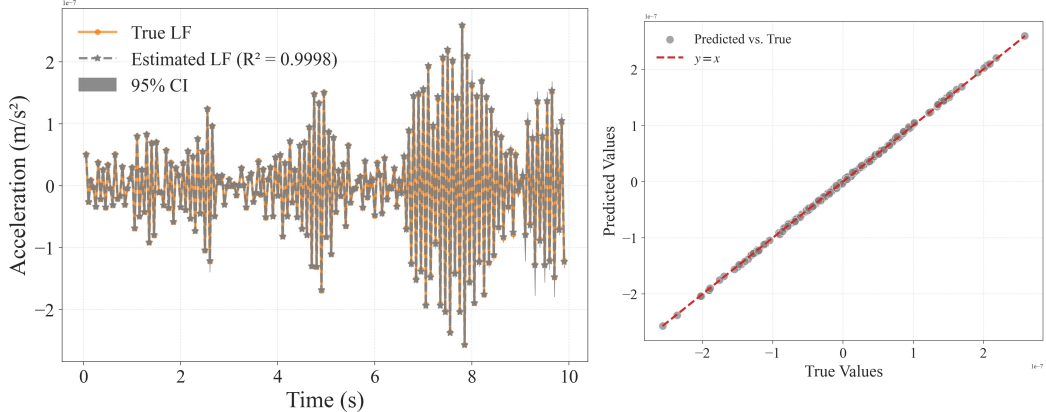


Figure 4: Validation of the LF model for Case 1.

Next, we proceed to train a MF model building upon the previously trained LF model. The LF model is used as a pre-trained initialization and subsequently fine-tuned using 180 available HF data pairs, while the remaining 20 HF data pairs are reserved for testing. The MF fine-tuning is performed for 500 epochs with a batch size of 16.

Fig. 5 and Fig. 6 show the true HF response and the MF model prediction for two test data pairs. In both figures, panel (a) compares the simulated HF and LF response for the corresponding inputs, while panel (b) compares the simulated HF response against the MF predicted mean with the associated 95% CI. For test dataset #1 (Fig. 5), the LF response reproduces the overall temporal trend of the HF data but deviates in amplitude and phase, particularly in the energetic burst around 7–9 s, leading to a moderate fit of $R^2 = 0.9607$. In contrast, the MF prediction achieves better agreement with the HF response ($R^2 = 0.9998$). The 95% credibility band is narrow across most of the time domain, indicating the reliability of predicted responses. For test dataset #2 (Fig. 6), the LF model again captures the general pattern but exhibits larger deviations at peak responses, reflected in a lower $R^2 = 0.9493$. The MF prediction, however, substantially improves the accuracy ($R^2 = 0.9974$), closely following both the amplitude and phase of the HF data. The uncertainty intervals also remain tight overall, reflecting appropriate credibility in prediction window.

Overall, the comparison between LF and MF demonstrates a significant improvement achieved by the proposed approach. While LF provides only an approximate proxy to HF dynamics, the MF model, through pre-training

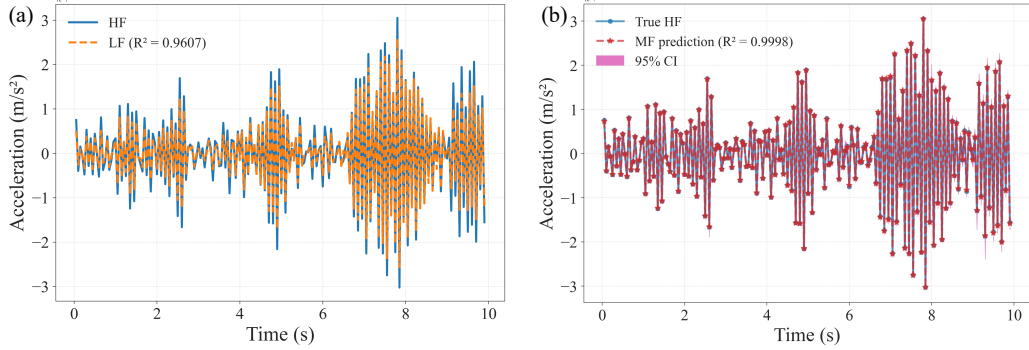


Figure 5: MF prediction performance on test data #1 for Case 1: (a) comparison between HF and LF simulated responses; (b) MF predicted mean and 95% compared against simulated HF response.

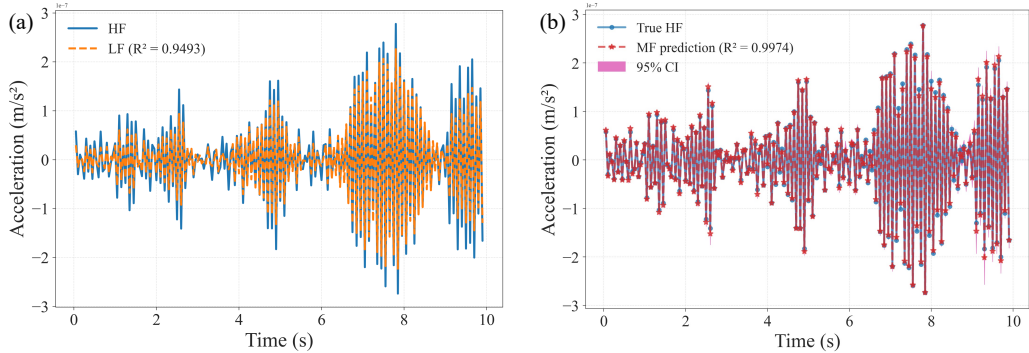


Figure 6: MF prediction performance on test data #2 for Case 1: (a) comparison between HF and LF simulated responses; (b) MF predicted mean and 95% compared against simulated HF response.

on abundant LF data and fine-tuning with limited HF data, learns an underlying representation that preserves critical features of the HF response. This enables accurate reproduction of both global trends and local transients, while providing reliable uncertainty quantification.

4.2. Case 2: weak correlation between HF and LF

In the second case, the LF and HF datasets exhibit a weaker correlation compared to Case 1 in Sec. 4.1. This weak correlation is intentionally introduced by increasing the discrepancy between the external excitations applied during LF and HF data generation. Apart from this modification, the modeling procedures remain identical to those in Case 1.

Fig. 7 illustrates a representative comparison between LF and HF accelerations. Unlike Case 1 (Fig. 3), where the LF and HF responses followed a similar pattern with relatively minor amplitude and phase mismatches, here the discrepancy between LF and HF data becomes much more pronounced. The LF data no longer provides a reliable approximation of the HF dynamics, particularly in high-energy segments where deviations in amplitude and phase accumulate over time. This intentionally degraded correlation setting poses a more challenging scenario for MF training and transfer learning. Since the LF data carry less direct information about the HF response, the MF model must rely more heavily on the fine-tuning process with limited HF data to achieve accurate predictions. As a result, Case 2 serves as a more stringent test of the proposed MF framework, demonstrating its robustness in situations where LF models are of limited fidelity and the LF–HF relationship is highly nonlinear and weakly coupled.

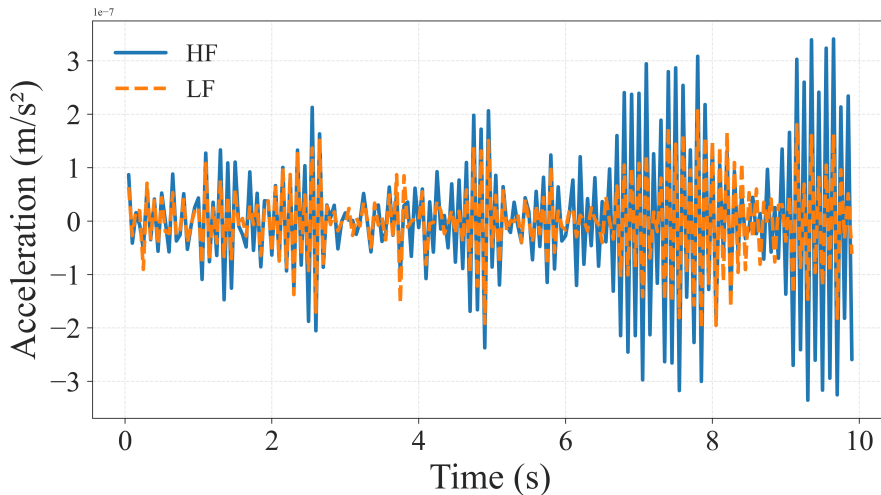


Figure 7: Example of simulated LF and HF acceleration responses for Case 2.

We again train the LF model using 980 LF datasets and 20 additional datasets for validation. Each dataset consists of 200 data points sampled over a 10-second duration. To ensure consistency with Case 1, the model architecture is taken to be the same. Specifically, the surjective NF model comprises seven flow layers with dimensionalities [200, 200, 200, 200, 10, 10, 10]. The first four layers are bijective and dimension-preserving, implemented through masked coupling flow. Dimensionality reduction is introduced at the fifth layer, where the representation is compressed from 200 to 10 using a

funnel architecture. The final two layers maintain this reduced dimension, thereby completing the flow.

Fig. 8 presents the validation performance of the trained LF model. On the left, the estimated LF response is compared against the true LF response. The two curves align closely across the full time window, yielding a high $R^2 = 0.9942$. The uncertainty band remains narrow, indicating that the LF model is also confident in its predictions. On the right, a point-to-point comparison between predicted and true LF data is shown, further confirming the excellent agreement between model predictions and simulated data. The results demonstrate that the LF surjective NF model provides reliable estimates of LF responses.

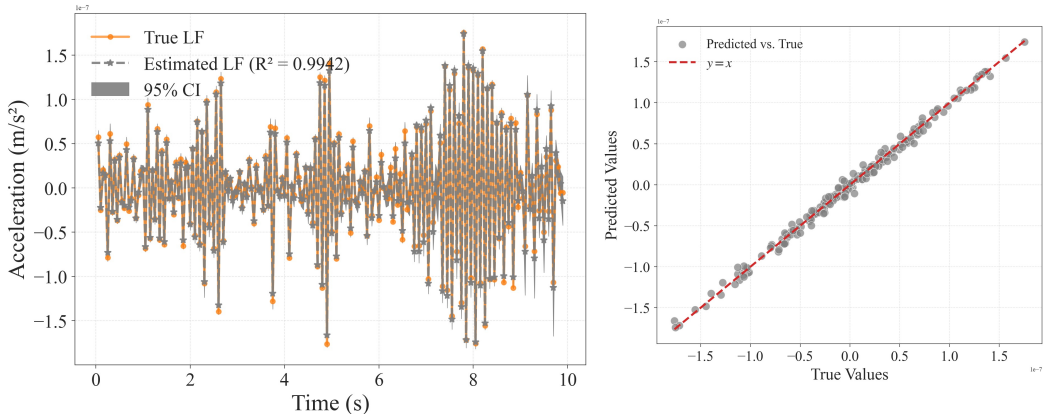


Figure 8: Validation of the LF model for Case 2.

We proceed to fine-tune the pre-trained LF model into the MF model by using 180 HF data pairs, with the remaining 20 HF data pairs are used for testing. Figs. 9 and 10 illustrate the MF prediction results for two test data pairs. In both figures, panel (a) compares the simulated HF and LF responses for the corresponding inputs. It can be seen that the LF responses deviate substantially from the HF responses, particularly in amplitude and phase during high-energy segments. This large discrepancy highlights the weak correlation between LF and HF in Case 2 and underscores the challenge of reducing such differences through MF learning. Panels (b) in Figs. 9 and 10 present the MF mean predictions and 95% CIs against the simulated HF responses. Despite the weak LF–HF correlation, the MF predictions align closely with the HF data across the entire time window, with R^2 values exceeding 0.99 in both cases. The 95% credibility bands remain generally

narrow, indicating a good prediction reliability. Importantly, the uncertainty widens in the final two seconds of the signal, where the HF responses exhibit stronger fluctuations. This behavior indicates that the predictive uncertainty increases in regions where the HF dynamics become more oscillatory and complex. The widening credibility bands capture this variability, ensuring that the MF model does not become overconfident in highly dynamic segments. Overall, these results confirm that the MF surjective NF model can successfully overcome weak LF–HF correlations, accurately recovering the HF dynamics while providing uncertainty estimates that adapt to the underlying structural response complexity.

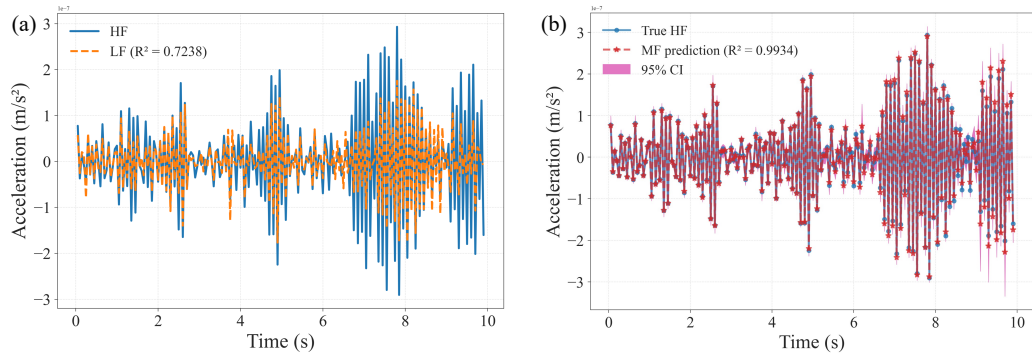


Figure 9: MF prediction performance on test data #1 for Case 2: (a) comparison between HF and LF simulated responses; (b) MF predicted mean and 95% compared against simulated HF response.

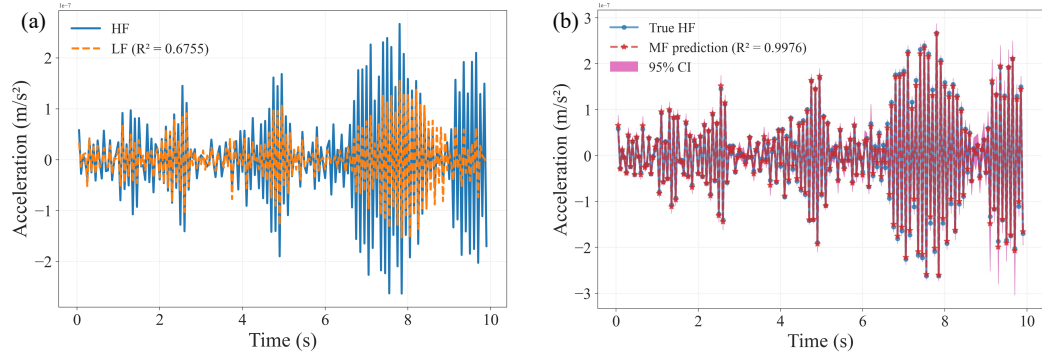


Figure 10: MF prediction performance on test data #2 for Case 2: (a) comparison between HF and LF simulated responses; (b) MF predicted mean and 95% compared against simulated HF response.

4.3. Effect of the amount of HF data

To further evaluate the robustness of the proposed approach, we investigate the effect of the number of HF data pairs used for fine-tuning on the performance of the MF model. Two additional scenarios are considered: (i) training a single NF model using only 180 HF data pairs without LF pre-training, and (ii) training a MF model using only 100 HF data pairs with LF pre-training as discussed in Secs. 4.1 and 4.2. Performance is quantified by the relative ℓ_2 error, defined as

$$\text{Relative } \ell_2 \text{ error} = \frac{\|\mathbf{y}_{\text{pred}} - \mathbf{y}_{\text{true}}\|_2}{\|\mathbf{y}_{\text{true}}\|_2}, \quad (25)$$

where \mathbf{y}_{pred} and \mathbf{y}_{true} denote the predicted and true HF responses, respectively. A smaller value indicates better predictive performance.

Figs. 11 and 12 present the results for Case 1 (strong LF–HF correlation) and Case 2 (weak LF–HF correlation), respectively, across three scenarios: HF-only (180 data pairs), MF with 100 HF data pairs, and MF with 180 HF data pairs. In both cases and for both test datasets, the consistent observation is that fine-tuning the LF model with 180 HF datasets yields the lowest relative ℓ_2 errors. By contrast, the HF-only model trained on 180 HF data pairs without LF pre-training consistently performs worst, confirming that the absence of LF information leads to poor overall performance. The MF model trained with 100 HF datasets provides intermediate performance, but still outperforms the HF-only baseline, underscoring the benefit of leveraging LF data through transfer learning.

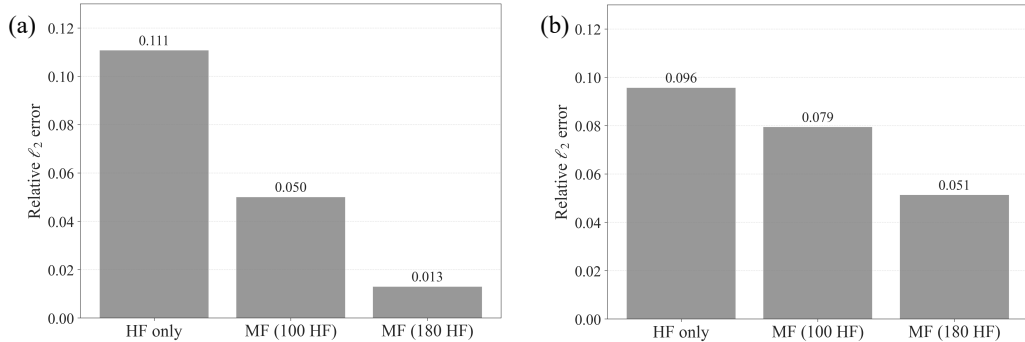


Figure 11: Effect of different amounts of HF data in Case 1 (strong correlation): (a) Test data #1; (b) Test data #2.

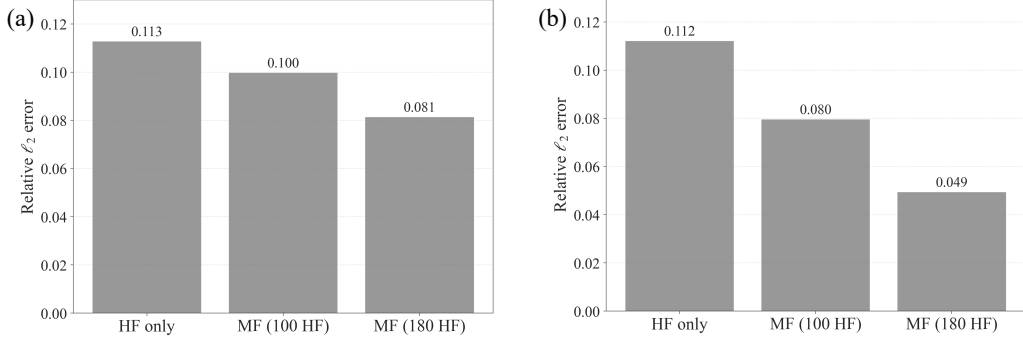


Figure 12: Effect of different amounts of HF data in Case 2 (weak correlation): (a) Test data #1; (b) Test data #2.

These results illustrate that the integration of LF knowledge is critical for efficient utilization of limited HF data. The MF model not only reduces the required number of HF datasets for training, but also delivers superior accuracy when fine-tuned with sufficient LF information. Furthermore, when the pre-trained LF model is used, incorporating more HF data significantly improves the predictive performance of the MF model. This trend highlights the complementary roles of LF knowledge transfer and sufficient HF information: the LF model provides a strong prior, while additional HF data refines the model to better capture the dynamics of the high-fidelity system.

4.4. Comparison against a conventional multi-fidelity ML approach

To further demonstrate the efficacy of the proposed MF surrogate modeling framework, we conduct a comparison against a traditional non-generative machine learning approach. In this study, we adopt the TCN as the backbone of the MF framework for comparison [15, 16]. TCN extends conventional convolutional neural networks (CNN) to sequential modeling by introducing causal convolutions and dilated filters, which allow the network to capture long-range temporal dependencies while preserving the ordering of time-series data. Owing to their efficiency and accuracy, TCN has been widely applied in time-series forecasting and sequence-to-sequence prediction tasks [29, 30].

In the MF surrogate setting, the TCN is employed in a manner analogous to the proposed flow-based model. Specifically, a LF surrogate is first trained using abundant LF data, and the pre-trained TCN is then fine-tuned to construct a MF surrogate using limited HF data. The input to the TCN consists of the structural model parameters concatenated with the time step,

such that the network predicts point-wise responses across the 200 time steps of interest. Unlike the generative flow-based framework, the TCN produces deterministic predictions without explicit uncertainty quantification. The TCN architecture adopted in this study takes 10 input features (9 model parameters and one time step) and predicts a single output at each time step. The temporal convolutional layers consist of 10 blocks, each with 60 channels, enabling the network to capture complex temporal patterns. A kernel size of 20 allows the receptive field to span longer sequences, while a dropout rate of 0.2 is introduced to mitigate overfitting. The comparison is carried out for Case 2, in which the LF–HF correlation is weak. This scenario is intentionally chosen because it represents the more challenging setting relative to Case 1 and therefore provides a stricter test of the proposed MF framework. For a fair comparison, the same 1000 LF and 200 HF data are used for training TCN.

Fig. 13 compares the prediction performance of the proposed framework against the TCN-based method for two HF test data pairs in Case 2. In both subfigures, the blue circles denote the true HF responses, the grey squares represent TCN predictions, and the red stars correspond to the proposed method. Overall, both methods are able to capture the general dynamic trends of the HF responses. However, the proposed framework demonstrates noticeably improved accuracy, as reflected in the smaller relative ℓ_2 errors (0.081 and 0.049 for the proposed method, compared to 0.103 and 0.092 for TCN in Fig. 13a and Fig. 13b, respectively). These improvements indicate that the proposed approach not only provides more accurate pointwise predictions but also better preserves the fine-scale temporal dynamics. The zoomed-in insets highlight regions where discrepancies are more evident.

While the TCN-based method exhibits slight phase mismatches and amplitude deviations from the ground truth, the proposed method remains closely aligned with the HF data. This demonstrates the advantage of the proposed probabilistic generative approach in learning complex temporal structures, particularly under weak LF–HF correlation settings where conventional deterministic ML methods such as TCN tend to degrade. Another key advantage of the proposed generative AI-enhanced MF modeling framework is that it produces full predictive probability distributions rather than point estimates as in the case of TCN, as shown in the shaded areas in zoomed-in insets representing 95% CIs. This capability allows the model to naturally quantify predictive uncertainty, which is critical for structural reliability assessment and risk-informed decision making. Furthermore, to

rigorously quantify predictive accuracy, we computed the average relative ℓ_2 errors between the MF prediction and the HF true data across 20 distinct, unseen test datasets for both the TCN and the proposed method. The TCN yielded a mean error of 0.091. In contrast, the proposed method achieved a lower average error of 0.0791 (12.7% reduction), indicates better accuracy and improved generalizability to unseen inputs.

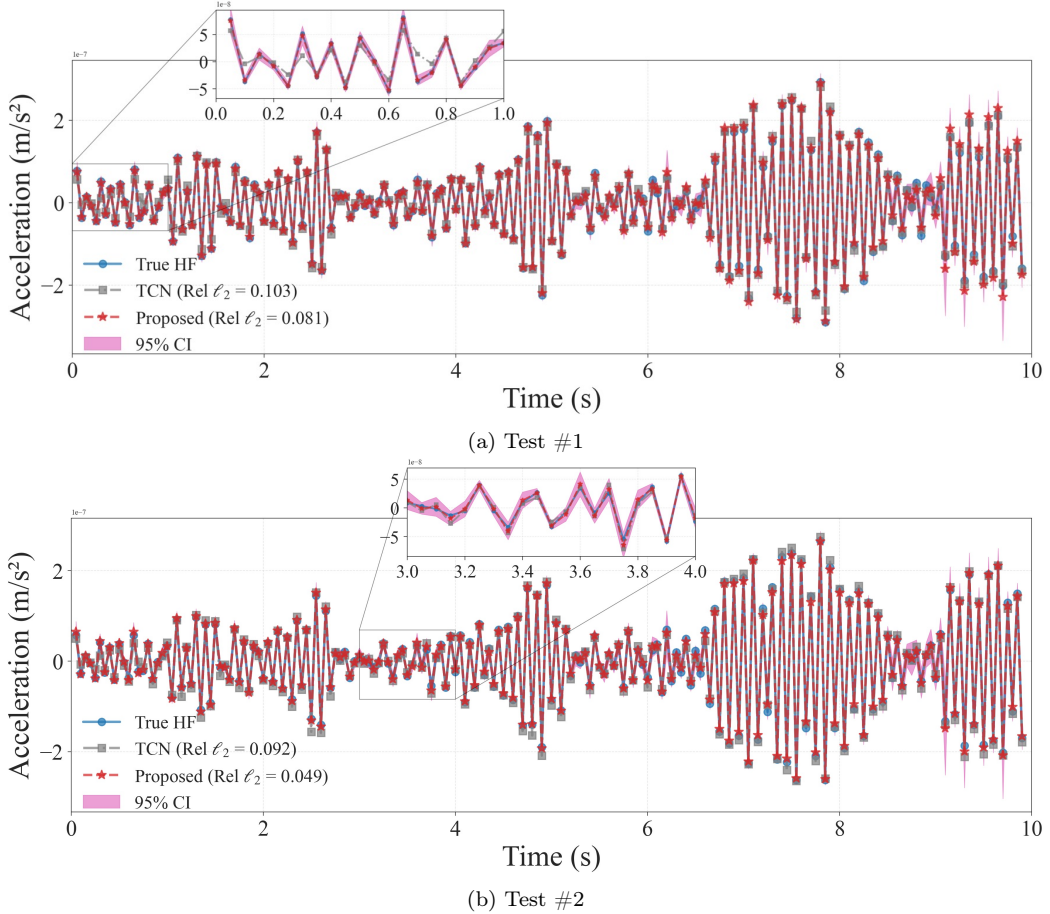


Figure 13: Comparison between the proposed method (predictive mean and 95% CI) and the TCN-based MF method for two test data examples.

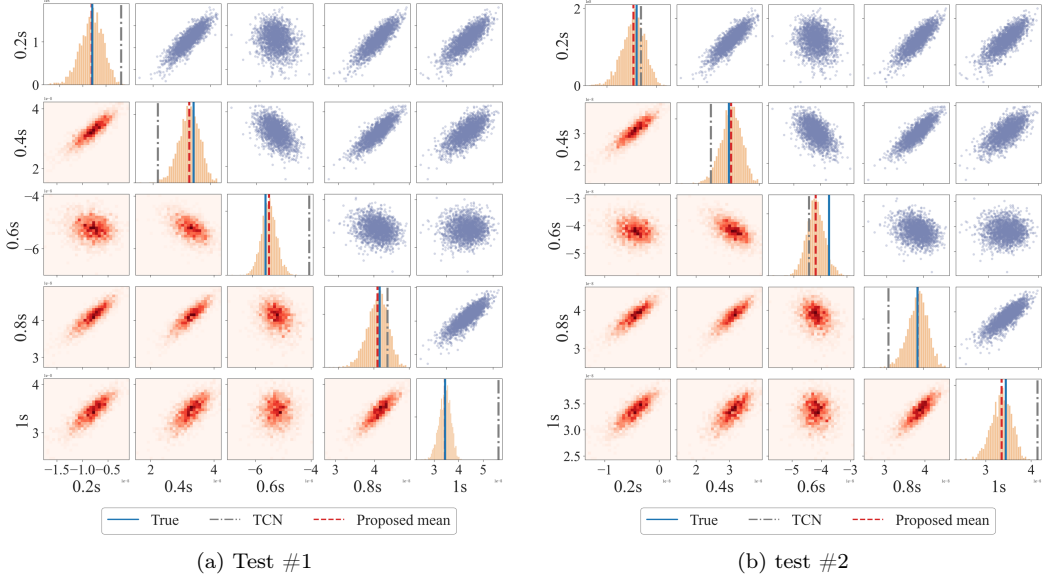


Figure 14: Probability distributions of predicted HF responses at selected time step for two test data examples.

Fig. 14 presents the estimated probability distributions at selected time instants ($t = 0.2, 0.4, 0.6, 0.8$, and 1.0 s) for two HF test data pairs. In each subplot, the histograms depict the probability distributions estimated by the proposed method, the gray dot-dashed vertical lines correspond to the deterministic predictions of TCN, and the red dashed vertical lines indicate the predictive means of the proposed method. The results demonstrate the clear advantages of the proposed framework. In several time steps, the TCN predictions noticeably deviate from the ground truth, indicating the limitations of deterministic point estimation. By contrast, the proposed method consistently provides predictive means that are well aligned with the true responses while simultaneously delivering full probability distributions. These distributions capture the variability of the HF responses and thus enable uncertainty quantification, offering a more reliable and informative representation of the system dynamics compared to conventional ML approaches.

5. Conclusion

In this study, we proposed a novel probabilistic MF surrogate modeling framework that integrates generative AI with transfer learning to address the significant challenge of scarce and expensive HF data. The framework

adopts a two-stage strategy: a generative surrogate is first pre-trained on abundant LF data, and the learned knowledge is then transferred via fine-tuning using limited HF data to construct a final MF model. The backbone of the framework is a conditional surjective NF model. Unlike traditional bijective NF that preserves dimensionality and thus struggle with high-dimensional response data, our framework incorporates a surjective layer (via a funnel architecture) that enables dimensionality reduction while retaining likelihood-based training. This design allows the model to efficiently handle high-dimensional structural responses for given structural model parameters as inputs, providing not only accurate predictions but also uncertainty quantification.

The effectiveness of the framework was demonstrated using a reinforced concrete slab example in two representative scenarios: strong LF–HF correlation and weak LF–HF correlation. In both cases, the proposed MF model exhibited strong predictive performance, accurately capturing the dynamics of high-dimensional time-series responses while providing reliable uncertainty estimates. Furthermore, an investigation on the effect of the amount of HF data used showed that fine-tuning the LF model consistently improves accuracy compared to training with HF data alone, underscoring the critical role of LF knowledge transfer when HF data is scarce.

The significance of this framework lies in its ability to combine generative modeling with transfer learning, enabling robust surrogate modeling under conditions of HF data scarcity. By explicitly quantifying uncertainty, our approach enhances the reliability of predictions, a feature that is essential for risk-informed decision-making in structural engineering. Future research will focus on extending this framework to more complex structural systems involving nonlinear and non-stationary dynamics. Additional directions include exploring adaptive multi-fidelity training strategies, incorporating physics-informed priors directly into the generative model, and applying the framework to real-world, large-scale structural health monitoring datasets.

References

- [1] H.-R. Bae, R. V. Grandhi, R. A. Canfield, Epistemic uncertainty quantification techniques including evidence theory for large-scale structures, *Computers & Structures* 82 (13-14) (2004) 1101–1112.

- [2] W. Zhao, Y.-M. Zhang, Reliability analysis of random vibration transmission path systems, *Mechanical Systems and Signal Processing* 113 (2018) 77–89.
- [3] J. Zeng, Y. Wang, A. M. Tartakovsky, D. A. Barajas-Solano, Solving high-dimensional inverse problems using amortized likelihood-free inference with noisy and incomplete data, *Computer Methods in Applied Mechanics and Engineering* 443 (2025) 118064.
- [4] J. Zeng, M. D. Todd, Z. Hu, Probabilistic damage detection using a new likelihood-free bayesian inference method, *Journal of Civil Structural Health Monitoring* 13 (2) (2023) 319–341.
- [5] Y. Zong, D. Barajas-Solano, A. M. Tartakovsky, Randomized physics-informed neural networks for bayesian data assimilation, *Computer Methods in Applied Mechanics and Engineering* 436 (2025) 117670.
- [6] J. Zeng, Y. H. Kim, S. Qin, Bayesian model updating for structural dynamic applications combining differential evolution adaptive metropolis and kriging model, *Journal of Structural Engineering* 149 (6) (2023) 04023070.
- [7] H.-P. Wan, W.-X. Ren, Stochastic model updating utilizing bayesian approach and gaussian process model, *Mechanical Systems and Signal Processing* 70 (2016) 245–268.
- [8] J. Kudela, R. Matousek, Recent advances and applications of surrogate models for finite element method computations: a review: J. kudela, r. matousek, *Soft Computing* 26 (24) (2022) 13709–13733.
- [9] D. Samadian, I. B. Muhit, N. Dawood, Application of data-driven surrogate models in structural engineering: a literature review, *Archives of Computational Methods in Engineering* 32 (2) (2025) 735–784.
- [10] M. Motamed, A multi-fidelity neural network surrogate sampling method for uncertainty quantification, *International Journal for Uncertainty Quantification* 10 (4) (2020).
- [11] B. Peherstorfer, K. Willcox, M. Gunzburger, Survey of multifidelity methods in uncertainty propagation, inference, and optimization, *Siam Review* 60 (3) (2018) 550–591.

- [12] D.-C. Feng, S.-Z. Chen, E. Taciroglu, Deep learning-enhanced efficient seismic analysis of structures with multi-fidelity modeling strategies, *Computer Methods in Applied Mechanics and Engineering* 421 (2024) 116775.
- [13] C. Stavropoulou, E. Katsidoniaki, N. Faedo, M. Göteman, Multi-fidelity surrogate modeling of nonlinear dynamic responses in wave energy farms, *Applied Energy* 380 (2025) 125011.
- [14] S. Yang, Y. Lee, N. Kang, Data-efficient deep operator network for unsteady flow: A multi-fidelity approach with physics-guided subsampling, *Computer Methods in Applied Mechanics and Engineering* 446 (2025) 118254.
- [15] Q.-M. Zhong, D.-C. Feng, S.-Z. Chen, Multi-fidelity enhanced few-shot time series prediction model for structural dynamics analysis, *Computer Methods in Applied Mechanics and Engineering* 434 (2025) 117583.
- [16] J. Zeng, G. Li, Z. Gao, Y. Li, S. Sundararajan, S. Barbat, Z. Hu, Machine learning enabled fusion of cae data and test data for vehicle crash-worthiness performance evaluation by analysis, *Structural and Multidisciplinary Optimization* 66 (4) (2023) 96.
- [17] G.-F. He, P. Zhang, Z.-Y. Yin, Active learning inspired multi-fidelity probabilistic modelling of geomaterial property, *Computer Methods in Applied Mechanics and Engineering* 432 (2024) 117373.
- [18] L. Wang, S.-P. Zhu, B. Wu, Z. Xu, C. Luo, Q. Wang, Multi-fidelity physics-informed machine learning framework for fatigue life prediction of additive manufactured materials, *Computer Methods in Applied Mechanics and Engineering* 439 (2025) 117924.
- [19] F. Xie, X. Zhang, S. Wu, T. Ji, Y. Zheng, Multi-fidelity bayesian neural networks for aerodynamic data fusion with heterogeneous uncertainties, *Computer Methods in Applied Mechanics and Engineering* 435 (2025) 117666.
- [20] Z. Wang, Q. She, T. E. Ward, Generative adversarial networks in computer vision: A survey and taxonomy, *ACM Computing Surveys (CSUR)* 54 (2) (2021) 1–38.

- [21] A. Iorliam, J. A. Ingio, A comparative analysis of generative artificial intelligence tools for natural language processing, *Journal of Computing Theories and Applications* 1 (3) (2024) 311–325.
- [22] G. Papamakarios, E. Nalisnick, D. J. Rezende, S. Mohamed, B. Lakshminarayanan, Normalizing flows for probabilistic modeling and inference, *Journal of Machine Learning Research* 22 (57) (2021) 1–64.
- [23] D. Nielsen, P. Jaini, E. Hoogeboom, O. Winther, M. Welling, Survae flows: Surjections to bridge the gap between vaes and flows, *Advances in Neural Information Processing Systems* 33 (2020) 12685–12696.
- [24] S. Dirmeyer, C. Albert, F. Perez-Cruz, Simulation-based inference for high-dimensional data using surjective sequential neural likelihood estimation, in: The 41st Conference on Uncertainty in Artificial Intelligence, 2023, p. none.
- [25] S. Klein, J. A. Raine, S. Pina-Otey, S. Voloshynovskiy, T. Golling, Funnels: Exact maximum likelihood with dimensionality reduction, *arXiv preprint arXiv:2112.08069* (2021).
- [26] L. Dinh, J. Sohl-Dickstein, S. Bengio, Density estimation using real nvp, *arXiv preprint arXiv:1605.08803* (2016).
- [27] S. Dirmeyer, Surjectors: surjection layers for density estimation with normalizing flows, *Journal of Open Source Software* 9 (94) (2024) 6188.
- [28] I. K. M. Jais, A. R. Ismail, Adam optimization algorithm for wide and deep neural network, *Knowledge Engineering and Data Science* 2 (1) (2019) 10.
- [29] P. Hewage, A. Behera, M. Trovati, E. Pereira, M. Ghahremani, F. Palmieri, Y. Liu, Temporal convolutional neural (tcn) network for an effective weather forecasting using time-series data from the local weather station, *Soft Computing* 24 (21) (2020) 16453–16482.
- [30] J. Fan, K. Zhang, Y. Huang, Y. Zhu, B. Chen, Parallel spatio-temporal attention-based tcn for multivariate time series prediction, *Neural Computing and Applications* 35 (18) (2023) 13109–13118.